Reconstructing Richtmyer–Meshkov instabilities from noisy radiographs using low dimensional features and attention-based neural networks

DANIEL A. SERINO,[1,*] MARC L. KLASKY,[1] BALASUBRAMANYA T. NADIGA,[1] XIAOJIAN XU,[2] AND TREVOR WILCOX[1]

[1]*Los Alamos National Laboratory, Los Alamos, NM 87545, USA*
[2]*Dept. of Electrical and Computer Engineering, University of Michigan, Ann Arbor, MI 48109*
[*]*dserino@lanl.gov*

Abstract: A trained attention-based transformer network can robustly recover the complex topologies given by the Richtmyer-Meshkoff instability from a sequence of hydrodynamic features derived from radiographic images corrupted with blur, scatter, and noise. This approach is demonstrated on ICF-like double shell hydrodynamic simulations. The key component of this network is a transformer encoder that acts on a sequence of features extracted from noisy radiographs. This encoder includes numerous self-attention layers that act to learn temporal dependencies in the input sequences and increase the expressiveness of the model. This approach is demonstrated to exhibit an excellent ability to accurately recover the Richtmyer-Meshkov instability growth rates, even despite the gas-metal interface being greatly obscured by radiographic noise.

1. Introduction

The ability to isolate precise material interfaces from radiographic images is of paramount importance in describing a broad array of physical phenomena including a number of hydrodynamic instabilities including the Richtmyer Meshkoff instability (RMI) [1,2], the Rayleigh Taylor instability [3–5], and the Kelvin–Helmholtz instability [6]. These phenomena arise in a broad range of situations from astronomical size events like supernova collapse [7], to microscopic events such as gas bubble sonoluminescence [8] and the supersonic combustion of ramjets [9]. Indeed, extraction of the peaks and troughs associated with these phenomena at the material interfaces, RMI in particular, is essential in capturing the growth rates and optimizing designs to mitigate these instabilities. Here we focus on the RMI that originates from the interaction of a shock wave with an interface separating two materials with different densities. In most cases an initial perturbation will be amplified following the passage of the shock. A deposition of baroclinic vorticity that is practically-instantaneous and results from a misalignment between the pressure gradient across the shock and the local density gradient across the interface leads to a subsequent (slower) growth of the perturbation.

While extensive examinations and reviews of the RMI have been performed over the past sixty years, most of of the experimental work to validate the RMI has been performed within shock tubes using rectangular geometry with gaseous or fluid materials, although some recent work has been performed in cylindrical geometry [10–16]. Additionally, some recent works have also examined the RMI in solid-solid settings to estimate the strength in ductile materials [17, 18].

The emergence of Inertial Confinement Fusion (ICF) as a potential power source has been a major impetus for the continued examination of the RMI [11, 12]. However, the spherical convergent geometry as well as large attenuation present in these experiments precludes previous analysis methods and diagnostics. For example, planar laser induced fluorescence, planar Rayleigh scattering, and particle image velocimetry. Consequently, examination of the RMI
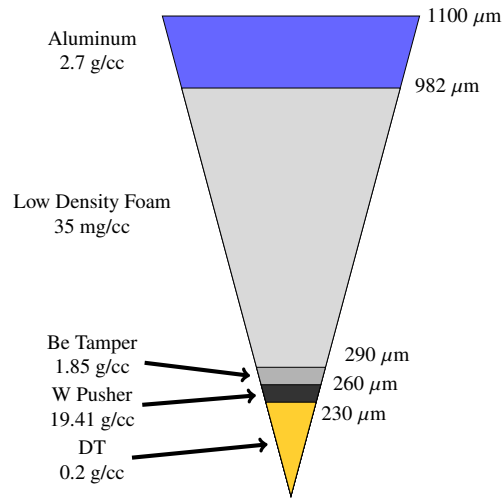
Fig. 1. Example double shell capsule specification based on the 1.06 MJ yield design from Ref. [19].
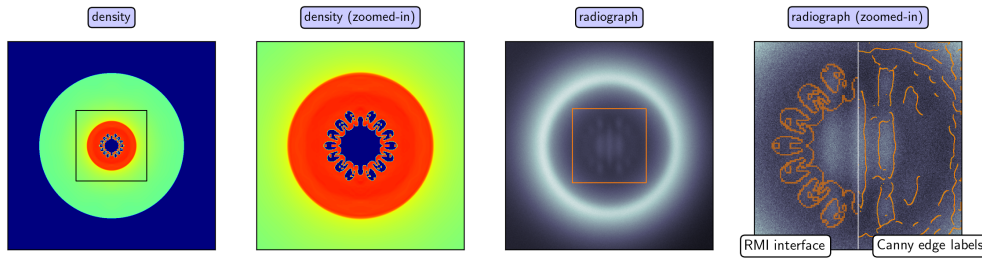

Fig. 2. Sample (r, z) projection of the density (1st column), zoomed-in view of the Richtmyer–Meshkov interface (2nd column), synthetic radiograph (3rd columns), and a zoomed-in view of the radiograph (4th columns) labeled with the RMI interface (left half) and Canny edge labels (right half).

instability in promising ICF concepts, such as the double shell capsules, depicted in Figure 1 demand the development of new experimental and analysis techniques to capture details of the RMI whose behavior and control are thought to be crucial for continued progress in ICF [11, 20]. That is, the RMI may induce mixing due on the interface between the outer shell and the inner fuel and in so doing inhibit the fusion reaction and can consequently be a limiting factor in the energy produced [21–24].

As an illustration in the difficulty in locating the interfaces necessary to quantitatively determine the RMI growth rates in spherical geometries, we present the result of a ICF hydrodynamic simulation in which a shock wave generated during the implosion of a nearly-spherical double shell capsule into a gas medium interacts with the irregular surface at the gas-metal interface during rebound to generate an RMI. It should be noted that this configuration is of particular interest in the proposed double shell ICF simulations as illustrated in Figure 1.

While the material interface in the hydrodynamic simulation is clearly observable and easily captured by applying traditional image processing methods, the observation from the noisy radiographic image makes the identification of the peaks and troughs (which are necessary to quantitatively characterize the growth rates of the RMI) problematic. Indeed, as may be observed

from Figure 2, traditional edge detection algorithms are generally insufficient to accurately find these features. Furthermore, these methods (Sobel, Canny, and Laplacian of Gaussian edge filters) generally require fine-tuning of hyper-parameters associated with the method, which may lead to significant uncertainty/error in the results. Finally, the sensitivity of the RMI to the initial characteristics of the perturbed surface further complicate the quantitative determination of growth rates.

This paper reports on the development of a new physics-based density reconstruction method capable of capturing, through a subsequent interface finding algorithm, RMI growth rates of ICF double shell implosions in a spherically convergent geometry using low dimensional features that are robustly identifiable from dynamic radiographic images. This approach may enable experimental validation in a regime that, to our knowledge, been largely unexplored.

2. Density Reconstruction via Dynamic Radiography

To examine the dynamic evolution of materials undergoing strong deformation in material science, shock physics, and ICF, dynamic radiography is routinely used as an experimental diagnostic [25–28]. Indeed, capturing the dynamic evolution of the material interface is essential in quantifying the growth rates of the RMI. As previously discussed, the limitations of traditional image processing algorithms require consideration of alternative techniques for capturing this interface with sufficient accuracy to infer the growth rates from noisy radiographs. One such technique for capturing the material interface is to use traditional density reconstruction techniques followed by applying gradient-based approaches to locate the material interfaces associated with the RMI growth rates. That is, an inversion of the projection data may first be performed to obtain the density field. Traditional methods of performing density inversions date back to Radon [29]. Over the past several decades, image reconstruction methods have evolved from simple analytical methods such filtered-back projection (FBP) methods, X-ray CT (e.g. Feldkamp-Davis-Kress or FDK methods), and the Inverse Abel Transform for axisymmetric systems [30–32] to models that enable inclusion of poly-energetic sources and also attempt to address the noise field (e.g. statistical noise as well as scatter). The models are complex non-linear, non-convex forward models and employ iterative reconstruction techniques [33]. Iterative reconstruction (IR) algorithms are based on more sophisticated models for the imaging system's physics and models for sensor and noise statistics. These methods are often called model based image reconstruction (MBIR) methods or statistical image reconstruction (SIR) methods [34]. Generally, density reconstruction algorithms using dynamic experimental radiographic data with complex noise fields (e.g., non-Gaussian noise, scattered radiation, complex beam dynamics, etc.) still encounter difficulty when sufficient accuracy is required to extract the intricate details necessary to characterize the RMI phenomena [28]. Furthermore, the nature of these methods introduces a certain degree of regularization that may impact the ability to accurately preserve edges. Research continues in this area to improve the ability to preserve edges in settings where uncertainty in the characteristics of scatter and noise are present [35–37].

More recently, machine learning (ML) approaches have been applied to radiographic reconstruction. Many of these ML architectures have outperformed IR methods by a large margin at a specified degradation level [38, 39]. Similar to traditional non-ML-based algorithms, ML-based approaches experience difficulty with complex noise fields. ML architectures that are trained using a specific noise distribution typically fail to obtain favorable results in the presence of out-of-sample noise [40, 41]. This problem can be partially addressed by training a number of models targeting each level of degradation. However, in many cases, the noise depends on the object and other imaging artifacts and therefore it is impractical to produce a general noise model to cover all unknown eventualities. In recent work [41], a machine learning-based Wasserstein generative adversarial network (WGAN) was developed to reconstruct density fields from noisy radiographic projections. This approach demonstrated excellent performance in reconstructing

density for testing cases that had the same noise properties as the training set. However, when testing noise levels outside of the training population, the reconstructions exhibited a rapid degradation in performance. Interestingly, degradation in performance was observed even when the noise level was reduced from the level used in the training.

In light of the inability to train a general denoising algorithm to address the issues associated with out-of-population noise and other imaging artifacts, we instead use a class of new ML-based methods that rely on features that are robustly identifiable from a series of dynamic radiographs. These methods are composed of two major components; one component is responsible for feature extraction, in this case the robust out-going shock, and another component performs density reconstructions from the extracted shock. This approach has been previously demonstrated on a relatively simple 1D system, where robust features were combined with the underlying hydrodynamic equations of motion to produce density reconstructions [28]. This methodology outperformed a traditional, direct radiograph-to-density reconstruction method in the presence of scatter. Furthermore, the method was also capable of generating families of solutions consistent with the observed features and a methodology for examining the uncertainty in the predictions was proposed.

To investigate the RMI we consider a test problem of shock propagation due to the implosion of a gas-filled ICF double shell capsule with a sinusoidal perturbation on the interior surface. Numerous simulations were performed with variable initial conditions and material parameters to produce a data set of density field sequences in time. Synthetic radiographs were produced for each time snapshot of density and a noise field was generated to mimic a realistic experimental setup. Ground truth features were generated using the density fields corresponding to coefficients of a curve fit for the shocks. We focused on a features-to-density network, for which we investigated two approaches including a generative variational autoencoder (VAE) approach called the ShockDecoderViT based on the vision transformer [42], and a deterministic structure-preserving model called the Mass-Conserving Transformer, based on the original transformer [43] to reconstruct the density fields to enable the subsequent extraction of the gas/metal interface and the RMI growth rates. Each architecture transforms a temporal sequence of features into their corresponding density fields using networks that incorporate attention layers. In previous work, attention blocks increased the expressive power of the networks by correlating temporal dependencies in the sequences [43]. In this paper, we demonstrate that incorporating attention in the features-to-density networks improves density reconstruction errors relative to a similar network without attention. The density fields are then processed to obtain the gas/metal interface to obtain the RMI growth rates.

To test the effectiveness of the features-to-density network in the full radiograph-to-density pipeline, we developed a noise model to characterize the errors of a feature extractor network. For the noise model, we used the results from a feature extractor network developed in [44] that consists of a convolutional neural network (CNN) with an image Fourier feature encoding (IFFE) layer. This network was trained on the noisy radiograph-to-features problem and is capable of recovering the shock features with sub-pixel accuracy. We trained the features-to-density network using noiseless features and applied the noise model during testing. We show that the features-to-density network remains robust in the presence of significant amounts of out-of-sample noise. Using the results of these ML methods, we investigated the limits of the radiograph-to-density pipeline in reconstructing the much higher dimensional phenomena present. Using the density fields we then assessed the ability of the ML method to reconstruct the gas metal interface attributed to the RMI with lower dimensional features, such as the outgoing shock captured from the radiographs. This pipeline provides a possible means to address the difficulty in validating simulations of 3D ICF double shell RMI experiments.

In the remainder of this work we present details of our new approach for performing density reconstructions and subsequent extraction of the gas-metal interface necessary for characterizing

RMI phenomena using the robust features extracted from the dynamic radiographic images. Section 3 introduces the dynamic radiography problem and model formulation. Section 4 introduces details of the hydrodynamic ICF test problem and data generation. Section 5 presents two machine learning approaches for determining the density fields from robust features identified from a dynamic radiographic sequence. Section 6 presents the results of the density reconstructions and ability to extract RMI growth rates using the ML architectures. Finally section 7 presents discussion of the simulation results and conclusions drawn from the numerical experiments.

3. Dynamic Radiography Problem Setup

Our objective is to recover the intricate details of the gas-metal interface by first estimating a time-series of densities $\{\rho_{t,i}(x)\}_{t=t_1}^{t_N}$, with $x \in \mathbb{R}^3$ and i representing a material index, from their corrupted radiographs $\{m_t\}_{t=t_1}^{t_N}$, where $m_t \in \mathbb{R}^{N_1 \times N_2}$ is a monochrome image with $N_1 \times N_2$ pixels. The times $t_1, t_2, ..., t_N$ denote N time points at which the radiographic measurements are collected. In this investigation we consider the axisymmetric problem, where density objects are fully characterized by the central slice through the near-spherical object. Following the determination of the density fields we then extract the gas-metal interface as described in Section 6.

Our imaging model may be described as follows: The areal density of the object along a ray r connecting the source and detector is denoted

$$\rho_{A_i}(r) = \mathcal{A}[\rho_i] = \int_{-\infty}^{\infty} \rho_i(r_x(u), r_y(u), r_z(u)) \, du, \tag{1}$$

where $\mathcal{A}$ is the forward operator corresponding to the Abel transform, $(r_x(u), r_y(u), r_z(u))$ is a parameterization of the ray r, $\rho_i(\cdot)$ denotes a time snapshot of a spatially varying density, and i is an index corresponding to the material being imaged. Using a simple measurement model of a mono-energetic X-ray source, the number density of photons reaching the detector along ray r is approximately given by

$$I(r) = I_0 \exp\left(-\sum_i \xi_i \rho_{A_i}(r)\right), \tag{2}$$

where I_0 is the number density of the incident beam and ξ_i is the mass attenuation coefficient of material i [45]. A discrete, finite radiograph is measured in practice representing a finite grid of detectors. This direct radiograph (without scatter) d at each detector pixel is approximated as

$$d[m,n] = \int_{R_{m,n}} I(r) \, dr \approx CI(r_{m,n}) \tag{3}$$

where $R_{m,n}$ denotes the rays impinging pixel (m,n), $r_{m,n}$ is the ray through the pixel center, and C is a constant that depends on factors such as the detector pixel area.

The transmission (noisy radiograph) includes contamination from several noise terms, and is given by

$$T_t = d_t + n_t, \tag{4}$$

where d_t and n_t are the direct radiograph and noise at time t. At each time, we model the noise as

$$n = D_{\text{dsb}} + D_{\text{s}} + B_{\text{s}} + \eta \tag{5}$$

where D_{dsb} represents the blur from the source and detector, given by

$$D_{\text{dsb}} = D_{\text{sb}} * \phi_{\text{db}}, \qquad D_{\text{sb}} = d * G_{\text{blur}}(\sigma_{\text{blur}}). \tag{6}$$

Here, ϕ_{db} is a custom kernel associated with the detector and $G_{blur}(\sigma_{blur})$ is a 2D Gaussian kernel with standard deviation σ_{blur}. In addition, the noise model includes correlated scattered radiation, D_s, and an uncorrelated linear tilted background scatter field, B_s, given by

$$D_s = \kappa d * G_{scatter}(\sigma_{scatter}), \qquad B_s = ax + by, \qquad (7)$$

where $G_{scatter}(\sigma_{blur})$ is a 2D Gaussian kernel with standard deviation $\sigma_{scatter}$, a and b are scalar constants, and x and y are projections of the 2D functions x and y to the image plane. Finally, both gamma and photon noise are added as

$$\eta = \eta^{Po}(\gamma_g) * \phi_g + \eta^{Po}(\gamma_p) * \phi_p. \qquad (8)$$

where η^{Po} is Poisson Noise and γ_g and γ_p are the rates and ϕ_g and ϕ_p are the gamma and photon kernels, respectively.

The choice to model scatter as a kernel convolved with the direct signal is common in the scatter correction literature [46, 47]. This approach provides a fast scatter model that is representative of models used in practice. The above model can be readily extended to polyenergetic X-ray sources [47, 48]. This work focuses on material objects that are of interest in double shell ICF capsules, and we work with monoenergetic X-ray sources for simplicity.

Great difficulty in performing the density time-series reconstruction arises due to the presence of scatter, noise, and additional factors including the variability of the beam spot, energy spectra, and model mismatch in the forward operator. Incorporating a time-series for the evolution of the underlying density fields over time could provide improved dynamic reconstructions [28, 49–52]. To this end we adopt a machine learning approach to incorporate hydrodynamic priors to encourage the estimated density time-series to be consistent with the equations of motion that govern their evolution.

The evolution of the density over time in a dynamic experiment can be modeled by a system of partial differential equations (PDEs) describing radiation hydrodynamics. To facilitate the analysis of the radiation-hydrodynamic system we utilize the Euler equations in a manner analogous to Bello-Maldonado. [53, 54] The system of PDEs comprise a continuum model governing density evolution and is applicable in many realistic scenarios where dynamic radiography is applied. A closure of the hydrodynamic variables in the form of a material-dependent equation of state (EOS) is required, along with appropriate initial and boundary conditions, to uniquely prescribe the time evolution of any hydrodynamic variable, including the density. In practice, the EOS and other conditions or parameters for a specific experiment or test case are usually unknown. In this case, directly using the PDEs to enable dynamic reconstruction is not feasible. In our study, we numerically integrate the Euler equations with varying choices of EOS model parameters to generate a large dataset of density time-series and learn an EOS-agnostic model for reconstructing densities.

4. Hydrodynamic Test Problem

4.1. Generation of Density Time Series

As a test problem, we study shock propagation in a time-dependent (3D) density profile, created by an implosion of a nearly-spherical ICF double shell configuration. The study is limited to azimuthal symmetry so that the density at any time can be described in cylindrical coordinates (r, z). Additionally we restrict our attention to the Mie-Grüneisen (MG) EOS model. Simulations are performed on a 440×440 uniform Cartesian grid on a computational domain given by the quarter-plane $[0, L] \times [0, L]$, where $L = 341$ μm. The uniform grid cell size is $\Delta r = \Delta z = \frac{440}{L}$. The metallic shell is made of Tantalum and its density is initially uniform at a value of 16.65 g/cc. The inner surface of the Tantalum can be described as the set of coordinates
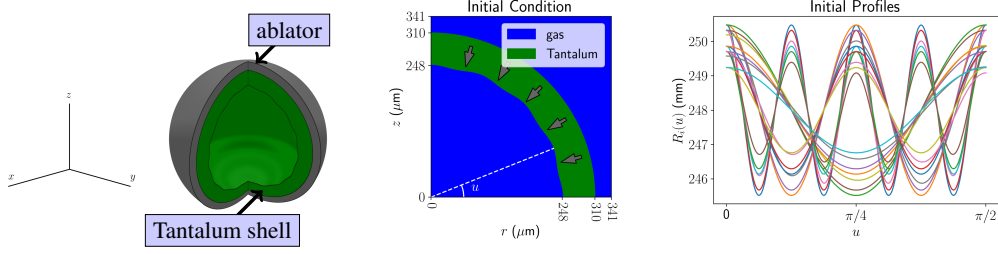
Fig. 3. Left: 3D mock-up of a Tantalum shell (green) with a perturbation on the interior surface and an outer ablator layer (gray). Middle: projection of the Tantalum shell onto (r, z) coordinates. The inner radius is parameterized by the angle, u, between the white dotted line and the r axis. The drive from the ablator is modelled as an initial velocity on the Tantalum shell (v_{impl}). Right: Plot of the 20 separate profiles for radius of the perturbed inner surface verses angle u.

$(r_{\text{in}}(u), z_{\text{in}}(u))$ satisfying

$$(r_{\text{in}}(u)^2 + z_{\text{in}}(u)^2)^{1/2} = R_{\text{in}} + \sum_{k=1}^{8} F_k \cos(2ku), \qquad u \in [0, \pi/2], \tag{9}$$

where $R_{\text{in}} = 248 \ \mu\text{m}$, F_k, $k = 1, \ldots, 8$, are coefficients of the perturbation corresponding to the kth cosine harmonic. The outer surface of the shell is a sphere with radius $R_{\text{out}} = 310 \ \mu\text{m}$. There are 20 different inner surface perturbation profiles considered in our dataset. The corresponding coefficients are recorded in Table 2. Figure 3 presents an initial perturbation given to the interior shell. As an initial condition, the shell is given a uniform implosion velocity, v_{impl}, in the direction of the origin to initiate an implosion.

In addition to varying the profile of the inner radius and the initial implosion velocity, our dataset consists of simulations covering parameters characterizing the MG equation of state [55],

$$p(\chi, T) = \frac{\rho_0 c_s^2 \chi \left(1 - \frac{1}{2}\Gamma_0 \chi\right)}{(1 - s_1 \chi)^2} + \Gamma_0 \rho_0 c_V (T - T_0), \tag{10}$$

where $\chi = 1 - \frac{\rho_0}{\rho}$, ρ_0 and T_0 are the reference density and temperature, respectively, c_s is the speed of sound, Γ_0 is the Grüneisen parameter at the reference state, s_1 is the slope of the linear shock Hugoniot curve, and c_V is the specific heat capacity at constant volume. Out of these parameters, we keep the reference density ρ_0 fixed at 16.65 g/cc and the reference temperature T_0 fixed at 0.0253 eV. The parameter set $\{c_s, s_1, \Gamma_0, c_V\}$ is varied as shown in Table 1.

Options	1	2	3	4	5
Γ_0	1.6	1.7	1.76	1.568	1.472
s_1	1.22	1.464	1.342		
c_s [m/s]	339000	372900	305100	355000	
c_V [erg g^{-1} eV^{-1}]	1.6×10^{10}	1.76×10^{10}	1.44×10^{10}		

Table 1. Matrix of parameter values used to develop the simulated dataset. All combinations of above parameters are used to simulate our data.

Altogether, the dataset realizes every unique parameter combination in a 7-dimensional parameter cube with 28, 800 total simulations. Each hydrodynamic simulation is comprised of
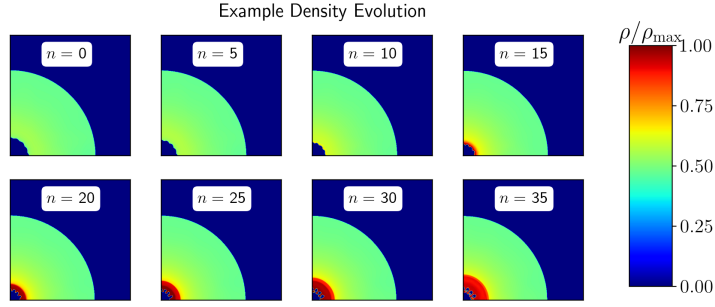
(a) Example of the density evolution for an initial condition with inner surface perturbation profile 1 for time indices $0, 5, \ldots, 35$. The images are 440x440 pixels representing the domain $[0, L] \times [0, L]$.
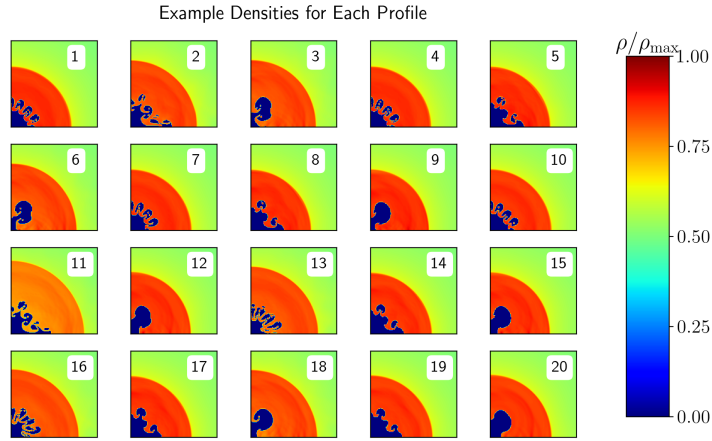
(b) Examples of the density at time index 40 for each inner surface perturbation profile. The images are 150x150 pixels representing the domain $\left[0, \frac{15}{44}L\right] \times \left[0, \frac{15}{44}L\right]$.

Fig. 4. Example plots of the density evolution (a) and the various RMI profiles representing each inner surface perturbation profile (b).

density field snapshots at later times when the instability is present. We label these times as $n = 0, 1, \ldots, 40$. An example of a density time series is shown in Figure 4. Once the Tantalum shell has collapsed, a shock is formed and reflected from the axis. The shock then interacts with the perturbed inner Tantalum edge. This creates an RMI. The topology of this interior evolves as depicted in Figure 4. The expanding shock proceeds to propagate into the non-constant dynamic density background. We chose frames corresponding to the time instants at $n = 25, 30, 35, 40$ to train the network in our studies.

4.2. Generation of Synthetic Radiographs

Synthetic radiographs are produced at each time step. The `create_sino_3d` function from the ASTRA Toolbox [56] is used to evaluate the forward operator in (1). Equation (2) is used to obtain the direct radiograph signal from the areal mass using $I_0 = 3.201 \cdot 10^{-4}$, $\xi_{(gas)} = 9.40$ cm^2/g, $\xi_{(Tantalum)} = \xi_{(coll)} = 13.03$ cm^2/g. The source blur kernel is a 2D Gaussian kernel with σ_{blur} chosen randomly between 1 and 3 pixels with a random orientation between 5 and 26 degrees. The correlated scatter kernel is also a 2D Gaussian kernel with $\sigma_{scatter}$ chosen randomly between 10 and 30 pixels and scatter level, κ, chosen randomly between 10 and 30. The coefficients of the
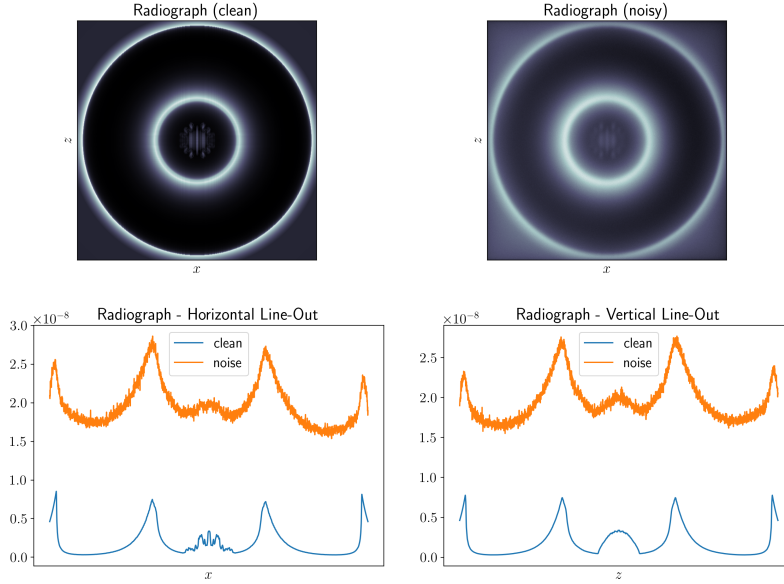
Fig. 5. Upper left: radiograph before applying noise. Upper right: radiograph after applying noise. Bottom left: horizontal line out through the center of the radiographs. Bottom right: vertical line out through the center of the radiographs. In both line plots, the orange line corresponds the noisy radiograph and the blue line corresponds to the radiograph without noise.

background scatter field are chosen such that the level is randomly between 0.5 and 1.5 times the mean signal level in the center of the image and the tilt is between -10% and 10%. The level of the gamma noise is randomly set in the range (39,000, 50,000) and the level of the photon noise is randomly set in the range (350, 450). Each random number is generated independently for each simulation and time step.

Figure 2 shows an example of a density field at time index 40 and a synthetic radiograph, m, generated using the above method. For the same example, Figure 5 shows the direct signal, d, radiograph m, and profiles across the center of the two images.

4.3. Generation of Shock Features

One of the primary aspects of the ICF shell dynamics is the evolution of the inner gas-metal interface, i.e., the growth of the instability. This is because the passage of the incoming and outgoing shocks through this interface renders it unstable to the RMI. Considering temporally evolving simulations, we are interested in times when the instability on this interface has permitted the growth of perturbations to the extent that the inner gas-metal interface displays significant asymmetry. As such, we assume that the interface as identified by the feature extraction procedure is not robust. That is, we expect that the interface as identified by the imaging and feature extraction procedures is sensitive to the dependent the measurement model. This is in contrast with the shock and outer edge features that we assume are robust. The robustness of these latter features is due to the symmetry of the setup and dynamics and the stable nature of their evolution. Nevertheless, because of its passage across the unstable inner gas-metal interface, we expect the stably evolving shock to be imprinted with a decaying set of perturbations that can be reliably identified.

Accordingly, we have extracted shock and edge features at each time for each sequence of

density fields. An edge-detection algorithm was utilized so as to enable the determination of a parametric representation of the shock and edge as a function of polar angle [28]. These features are subsequently compressed into a low-dimensional representation in terms of cosine harmonic coefficients,

$$r^{(i)}(\theta) = \sum_{j=0}^{N^{(i)}} F_j^{(i)} \cos(2j\theta), \tag{11}$$

for $i = \text{shock, edge}$. We found that $N^{(\text{shock})} = 8$ and $N^{(\text{edge})} = 5$ can represent the shock and edge features with sufficient accuracy across the dataset.

4.4. Noise Model for Feature Extraction

The focus of this paper is to develop a features-to-density network to be used as the second component in a radiograph-to-features-to-density pipeline for the purpose of quantifying the growth rates of RMI in double shell ICF environments. For simplicity and modularity, we built each component independently, where the feature extractor was trained on radiograph and feature data pairs and the features-to-density network was trained on feature and density data pairs. To test the performance of the trained features-to-density network, we developed a noise model to simulate the errors that would arise from the feature extraction model.

The feature extraction model is a CNN consisting of an image Fourier feature encoding (IFFE) layer, convolution layers, and fully connected layers. The feature extractor is applied to a subset of the synthetic radiographs. Errors between the reconstructed cosine harmonic coefficients and that of the ground truth were calculated and used to compute a sample mean and covariance matrix for the shock. Using these computed statistics, we simulated the error produced from reconstructing the cosine harmonic coefficients from synthetic radiographs using a multivariate Gaussian noise model. During model testing, we added noise consistent with this distribution to the inputs to better characterize the performance of the model.

5. Description of Features-to-Density Architectures

We compared two different architectures for solving the features-to-density problem. These approaches involve a generative variational autoencoder (VAE) network based on the vision transformer [42], which we refer to as the ShockDecoderViT, and a deterministic structure-preserving network based on the original transformer [43], which we call the Mass-Conserving Transformer. Due in part to the presence of radiographic noise, the features identified by the radiograph-to-features network can only be determined up to a certain level of precision. The two networks have different approaches for handling this uncertainty. The generative approach builds uncertainty into the model and is trained to minimize degeneracy of the density reconstructions. The deterministic network uses mass-conservation to improve robustness of predictions.

Both architectures are trained on the features-to-density problem using data at time steps $n = 25, 30, 35, 40$. The training set consists of 80% ($N = 23{,}040$) randomly selected density time series for each inner surface perturbation profile and the testing set consists of the remaining 20% ($N = 5{,}760$) of data. Since most of the action is downstream of the outgoing shock, we primarily restrict our attention to reconstructing a smaller region encapsulating the gas metal interface. For purposes of comparison, the architectures were trained to output a 150×150 square pixel image representing the density field in the cylindrical domain, $\left[0, \frac{15}{44}L\right] \times \left[0, \frac{15}{44}L\right]$. This smaller domain window captures the most interesting physics. Additionally, the Mass-Conserving Transformer architecture was trained to output a 440×440 square pixel image representing the full domain of the simulation data, $[0, L] \times [0, L]$.

5.1. ShockDecoderViT: A Vision Transformer-based Shock Decoder

We propose a new generative architecture to decode the density field from the shock features based on the vision transformer [42] and a conditional variational autoencoder (cVAE) learning framework [57–59]. In particular, the data consists of the density field $\rho(t)$ and a corresponding small number of numeric features characterizing the shock $\mathcal{F}(t)$ at four times in a dynamically evolving flow. The aim is to obtain a trained model (in this case just the decoder part of the cVAE) that, given a set of time evolving shock features alone—the conditions, generates a sequence of 2D density fields at the corresponding times. We call the decoder a ShockDecoderViT because the details of the flow can be reconstructed given a minimal set of shock characteristics. In common with most current ML approaches, the utility of this model is largely restricted to the training data distribution.

The cVAE consists of an encoder and a decoder. First, the encoder embeds the input images and conditions and processes them using the transformer. Here ideas of the vision transformer are used to process the density field. That is, the density field is considered as an image that is first split into patches which serve as tokens. In the present setting, only the region interior of the outermost extent of the outgoing shock is considered for the reason that most of the rapid and large dynamical changes are confined to this region. In particular, the interior most 150×150 region is partitioned into 10 patches of size 15×15. The patches and the conditions, which are taken to be the zeroth through seventh cosine harmonics of the outgoing shock at the four times, are then projected onto the tokens' embedding space. After adding positional encoding to the projections, dot-product attention-based transformer blocks are applied to obtain a compact variational latent space representation of the temporal sequence of densities and shock features at the bottleneck. That is, the encoder produces the mean $\mu(\rho(t), \mathcal{F}(t))$ and variance $\Sigma(\rho(t), \mathcal{F}(t))$ of the latent space features as functions of density and shock features. Thereafter, the decoder takes inputs of the latent variables realizations and the shock features and embeds them into a series of tokens that are processed using attention-based transformer blocks before they are projected back into density space.

The transformer-based encoder and decoder (ShockDecoderViT) of the cVAE are trained simultaneously with the Evidence Lower Bound (ELBo) of variational inference as the loss function. This loss function may be thought of as having two components: the reconstruction loss of the autoencoder and the KL divergence between the latent distribution produced by the encoder and a standard multivariate normal. In the testing phase, only the decoder is used; it takes as input the shock features. The shock features are combined with random realizations of the latent space variables to then generate the density fields.

In summary, our new architecture, the ShockDecoderViT, combines the strengths of the dot product attention-based Vision Transformer and the conditional variational autoencoder to generate temporally coherent sequences of density fields from dynamically evolving sequences of shock features. While the patch-based approach allows it to handle large images efficiently, the transformer provides the ability to capture long range dependencies in both the spatial and temporal domains. Results are presented for an architecture that uses two transformer blocks in the encoder and eight transformer blocks for the decoder. Increasing the number of encoder transformer blocks and small variations of the number of transformer blocks in the decoder led to minor changes in results (not shown).

5.2. Mass-Conserving Transformer Architecture

In addition to considering the ShockDecoderViT, which is a generative network, we also investigated a purely deterministic architecture. The Mass-Conserving Transformer network is a structure-preserving architecture that uses the transformer blocks introduced in [43]. While the ShockDecoderViT uses a vision transformer in both the encoder and decoder to go between latent representations and density field image patches, the Mass-Conserving Transformer treats

the input shock features using a series of transformer blocks before projecting to density. The network uses a mass-conservation layer to enforce that the dynamics conserve mass between time steps.

The input to the Mass-Conserving Transformer is a matrix $x \in \mathbb{R}^{N_t \times N_f}$, and the output is $y \in \mathbb{R}^{N_t \times N_r \times N_z}$. N_t is the number of times in the sequence, N_f is the total number of features, which consists of shock features a temporal encoding vector which represents polynomials in n, n^i, for $i = 0, 1, \ldots N_p$, and $N_r \times N_z$ is the resolution of the output image. The shock features are each centered and normalized using the mean and standard deviation of the training set.

The features are first inputted into a network consisting of multiple transformer blocks,

$$\chi = T_B \circ \cdots \circ T_1(x), \tag{12}$$

where $\chi \in \mathbb{R}^{N_t \times N_f}$ is a matrix representing a latent representation of the density fields at each time in the sequence. The transformer blocks have the same structure as the blocks proposed in [43]. Each block applies dot-product attention to incorporate temporal dependencies.

After the series of transformer blocks, the latent variables are projected into density fields. A critical component of projection step is the learning of characteristic eigenfunctions, $\mathcal{Z}^{(i)} \in \mathbb{R}^{N_r \times N_z}$, for $i = 1, \ldots, N_{\mathcal{Z}}$ on the image plane. The first set of transformations is given by

$$\mathcal{Y}_{ij}^n = h\left(\mathcal{Z}_{ij}^{(1)}, \ldots, \mathcal{Z}_{ij}^{(N_{\mathcal{Z}})}; \theta_n\right), \qquad i = 1, \ldots, N_r, \quad j = 1, \ldots, N_z, \quad n = 1, \ldots, N_t, \tag{13}$$

where h is a feedforward neural network parameterized by weights, θ_n, which are in turn determined by

$$\theta_n = g(\chi_n), \qquad n = 1, \ldots, N_t, \tag{14}$$

where g is also a feedforward neural network. The intermediate output, $\mathcal{Y} \in \mathbb{R}^{N_t \times N_r \times N_z}$, represents a sequence of images with the same resolution at the final output y. The reconstructed density is obtained by passing the sequence, $\mathcal{Y}^n$, $n = 1, \ldots, N_t$, through a mass conservation layer. Let $\mathcal{M}$ be the total mass of the object and let

$$M(\gamma) = \sum_{i,j} 4\pi r_i \gamma_{ij} \Delta r \Delta z, \tag{15}$$

be the calculation of mass of in the image γ, where r_i is the radius at index i and γ_{ij} is the density value in pixel (i, j). The output density reconstruction is the sequence of images

$$y^n = \frac{\mathcal{M}}{M(|\mathcal{Y}^n|)} |\mathcal{Y}^n|, \qquad n = 1, \ldots, N_t. \tag{16}$$

Our architecture used 6 consecutive transformer blocks, $B = 6$, each with 8 heads, $H = 8$, a latent dimension of 64, $k = 64$, and a feedforward neural network with inner dimension 2048 and tanh activation function. For the projection layer, we chose $N_{\mathcal{Z}} = 40$ eigenfunctions and represented both g and h using feedforward neural networks with 2 hidden layers and latent dimension of 100. The architecture was trained to minimize the root-mean-squared error (RMSE) of the density reconstructions on the training set.

6. Results

This section presents results of the trained ShockDecoderViT and Mass-Conserving Transformer networks. First we compare the two approaches using ensemble metrics such as root-mean-squared error (RMSE) and structural similarity. Section 6.1 examines the generative nature of ShockDecoderViT. Section 6.2 analyzes the density reconstructions of each inner surface

perturbation profile and its corruptions due to errors arising from the radiograph-to-features network. Additionally, we use an example reconstruction to demonstrate how peak-to-trough evolution can be calculated accurately, as indicated by capturing the RMI growth rates from the reconstruction and comparing to those obtained from the ground truth simulations.
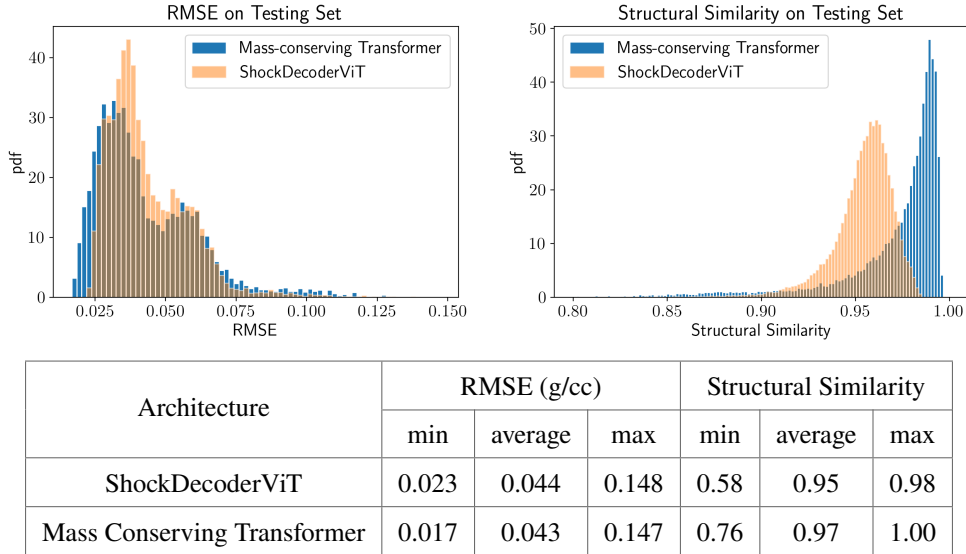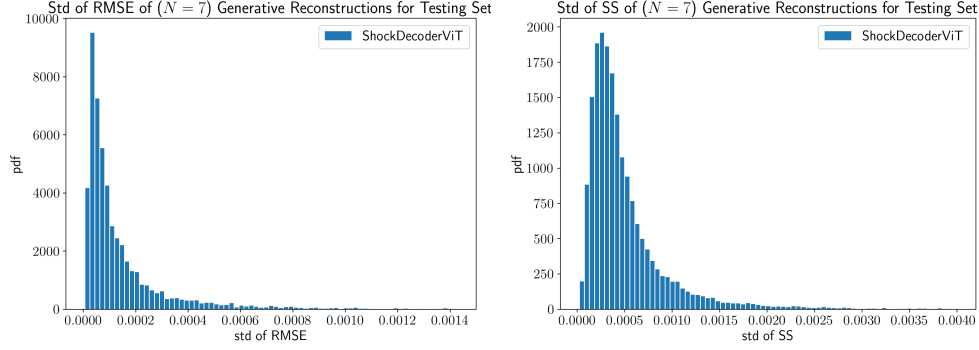

Architecture	RMSE (g/cc)			Structural Similarity		
	min	average	max	min	average	max
ShockDecoderViT	0.023	0.044	0.148	0.58	0.95	0.98
Mass Conserving Transformer	0.017	0.043	0.147	0.76	0.97	1.00

Fig. 6. Histogram of root-mean-squared errors (RMSE) (top left) and structural similarity (top right) between the density reconstruction and ground truth for the testing set for the ShockDecoderViT and Mass-conserving transformer. Bottom: table of summary statistics for the above histograms.

Figure 6 shows histograms of RMSE and structural similarity evaluated on the testing set for both architectures along with a table of summary statistics. Both networks exhibit similar performance in RMSE, with the Mass-Conserving Transformer having better minimum, average, and maximum errors compared to the ShockDecoderViT. The Mass-Conserving Transformer significantly outperforms the ShockDecoderViT in structural similarity, with a mode shifted to the right and better minimum, average, and maximum structural similarity values.

6.1. ShockDecoderViT Density Reconstruction

This section examines the generative nature of the ShockDecoderViT network. For each set of shock features in the testing set, we generated $N = 7$ realizations of density reconstructions using the ShockDecoderViT and computed the standard deviation of the density, RSME, and structural similarity. Figure 7 summarizes the results of this study, showing histograms of the standard deviations of both RMSE and structural similarity, along with summary statistics in a table. The variation in the RMSE and Similarity metric are very small relative to the ensemble averages, indicating that the variations due to the degeneracy are small. We reiterate that the standard deviation of deterministic methods, including the Mass-Conserving Transformer, on a fixed input is zero by definition.

Figure 8 shows examples of generations from six sets of shock features. These six features were chosen to correspond to the extremities of the standard deviation histogram, minimums, averages, and maximums for the standard deviation of RMSE and structure similarity. For each set of features, we chose the best, average, and worst performing reconstruction to display. Additionally, the standard deviation of density is shown in the last column. For the best and

Fig. 7. Histogram of the standard deviation of RMSE (left) and SS (right) for $N = 7$ generations of each example in the testing set. Bottom: table of summary statistics for the above histograms.

average examples, the reconstructions are nearly identical under visual inspection, while the worst performing reconstruction exhibits significant errors from the ground truth and are visually different from the other reconstructions in the example. This is also confirmed by examining the large values present in the density standard deviation heat map. This extreme example is however one example of a number of outliers represented by the narrow wide tail of the histogram in Figure 7.

6.2. Mass-Conserving Transformer Density Reconstruction

This section analyzes the density reconstructions produced by the Mass-Conserving Transformer network. Figure 9 shows the training loss, representing RMSE over the training set, verses the training epoch. The trained model was used to produce the density reconstructions and their corresponding errors shown in Figure 10. Each example reconstruction in this figure, labeled 1 through 20, corresponds to a different set of shock features, chosen randomly, corresponding to each inner-surface perturbation profile. The labeled structural similarity and RMSE were computed for the ensemble of testing data for each profile. The top plot (a) displays the density reconstructions sorted from lowest to highest structural similarity. The bottom plot shows the corresponding errors of the above plot, labeled by profile ensemble average RMSE in g/cc. Despite the low dimensional feature space, the density, including the complex details of the RMI, can be reconstructed to a high level of accuracy.

   Next, we investigated the effect of errors from the radiograph-to-features network on the Mass-Conserving Transformer results. For each set of shock features in the testing set, a random error is generated using the noise model described in Section 4.4. Reconstructions were produced for this generation of random error multiplied by factors of $0, 1, \ldots, 19$, respectively, and the corresponding RMSE was computed. Figure 11 shows box plots summarizing the error statistics of this study for each noise multiplier. A clear degradation in accuracy is observed as the noise multiplier is increased. For the case of $1\times$ multiplier, which corresponds to the expected error produced from the radiograph-to-features network, the boxplot represents a small shift from the clean features. The trend towards greater noise remains gradual and bounded, demonstrating the
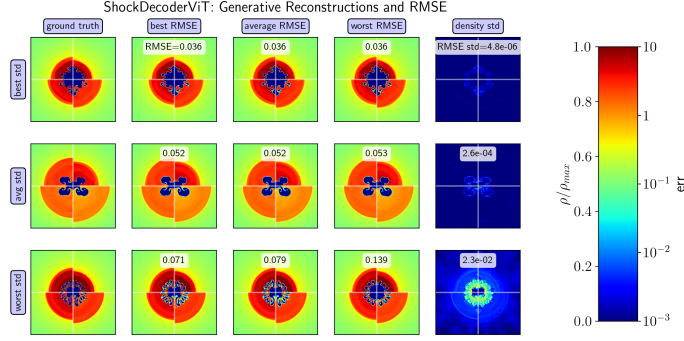
ShockDecoderViT: Generative Reconstructions and RMSE

(a) Multiple generative reconstructions for examples with the lowest (top row), average (middle row), and highest (bottom row) standard deviation in RMSE.

ShockDecoderViT: Generative Reconstructions and Structural Similarity
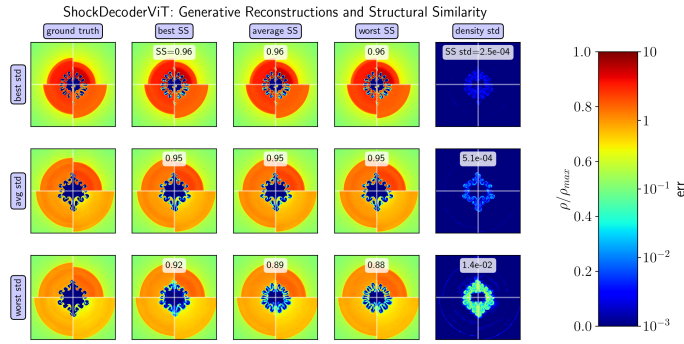
(b) Multiple generative reconstructions for examples with the lowest (top row), average (middle row), and highest (bottom row) standard deviation in SS.

Fig. 8. Examples of generative reconstructions produced by the ShockDecoderViT corresponding to the lowest, average, and highest standard deviation in RMSE (a) and Structural Similarity (b). In both sub-figures, the left-most column is the ground truth, the middle three columns correspond to the best, average, and worst errors, and the right-most column shows the standard deviation in density for the $N = 7$ generative reconstructions for the corresponding case. Each plot shows quarter planes corresponding data at each of the four times in the sequence counter-clockwise from the first quadrant.

robustness of the model, which may be attributed to it's structure-preserving properties.

Next, we studied the expressive power of the attention mechanism used in the Mass-Conserving transformer. By default, the dot product attention represents a fully connected network between each of the 4 terms of the sequence. For comparison, we also considered a sequence length 1 network, formed by breaking all the cross-temporal connections of the network, and a sequence length 2 network, formed by breaking the cross-temporal connections between the first two times and the latter two times. Figure 12 shows the training loss of the three approaches. The results indicate that incorporating more temporal correlations led to smaller training losses.

While our previous results focused on reconstructing density in a smaller region around the RMI, we also demonstrate that our approach can be applied to reconstruct the density in the entirety of the domain using the Mass-Conserving Transformer. A new model was trained using the full 440×440 domain available in the data set to produce a new set of architecture weights. The two plots in Figure 13 show histograms of RMSE and structural similarity evaluated on the
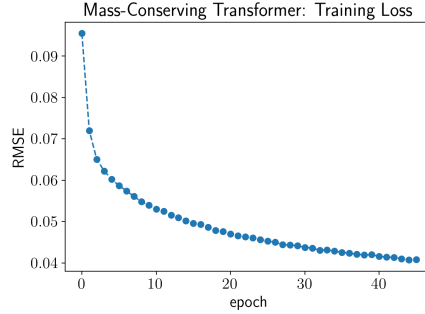
Fig. 9. Root mean squared error verses epoch during training.

testing set. We observe that the complexities of the gas metal interface are still reconstructed by the full domain model. Figure 15 shows an example of density reconstructions and corresponding horizontal and vertical line-outs through the center and Figure 14 shows a zoomed in view of the reconstruction and its error. In these examples, the RMI and shock location are still captured accurately.

Next, we demonstrate that the Mass-Conserving Transformer can accurately measure properties of the RMI such as the growth of the peak-to-trough radial distance. We chose a set of shock features, applied a random perturbation generated from the noise model of the radiograph-to-features network, and performed a density reconstruction. First we identified pixels that are contained in the gas domain, which is contained in a region near $(r, z) = (0, 0)$, which corresponds to a region of significantly lower density compared to that of the surrounding metal. A discontinuity separates the interface between the gas and metal. On both sides of the discontinuity front, the densities are approximately constant. In the reconstruction, there is a small region consisting of less than a few pixels where the density transitions smoothly between the nominal fluid density and the nominal solid density. Therefore, we attempt to split the difference. We find the maximum density of the metal, ρ_{max} and take the fluid domain to be the region where the density is less than $\frac{1}{2}\rho_{max}$. From this, we identify the pixel locations on the edge of the domain with the furthest and closest distances to the origin. Figure 16 shows the result of this identification algorithm applied to both the reconstruction and the ground truth for two examples of RMI profiles, representing high and low frequency modes. Additionally, we apply a Canny edge filter for various choices of the smoothing and threshold parameters to the noisy radiograph to identify the peak and trough of the RMI. Figure 16 shows a line plot comparing the peak-to-trough evolution between the ground truth, the reconstruction, and Canny edge filter. The density reconstruction approach is successful in accurately identifying the peak and trough locations and consequently their radial distance. The Canny edge filter however is unable to obtain an acceptable level of accuracy and suffers from large variations due to choices in meta-parameters. Figure 2 shows the resulting edges that are detected for the high frequency profile (profile 1). This demonstrates that our density reconstruction algorithm is a viable approach for making growth-rate estimates in the evolution of a spherically-symmetric RMI. We cannot overemphasize the importance of this discovery. That is, this method of reconstruction may allow the RMI growth rates to be experimentally verified in a spherically convergent geometry for the first time.

7. Conclusions

This work presents a new density reconstruction approach that uses a trained attention-based transformer network to enable accurate density reconstructions from a series of noisy radiographic

images. The key component of this network is the transformer encoder that acts on a sequence of features extracted from noisy radiographs. This encoder includes numerous self-attention layers that act to learn temporal dependencies in the input sequences and increase the expressiveness of the model.

The two architectures had comparable performance, with the Mass-conserving Transformer slightly outperforming the ShockDecoderViT. Furthermore, the shock harmonic features provided sufficient constraints to limit the variability in the density predictions, with variations that are insignificant compared to the mean reconstruction errors.

Our examinations also indicated the benefit of the dynamics relative to the traditional approach of reconstruction of single images. Finally, we demonstrated the ability to use our sparse features to accurately reconstruct the fine features of the image, enabling, for the first time, the determination of the RMI growth rates. This work opens the potential to experimentally capture RMI growth rates in spherical geometries.

A.   Cosine Coefficients for Inner Surface Perturbation Profile

The coefficients of the cosine harmonic series of the initial inner surface perturbation profile is scaled according to $F_i = R_{in}\bar{F}_i/8$, for $i = 0, \ldots, 8$, where $\bar{F}_0 = 8$, $\bar{F}_5 = \bar{F}_7 = 0$, and the rest of the coefficients are provided by Table 2.

Disclosures.   The authors declare no conflicts of interest.

Data Availability Statement.   Data underlying the results presented in this paper are not publicly available at this time but may be obtained from the authors upon reasonable request.

References

1. R. D. Richtmyer, "Taylor instability in shock acceleration of compressible fluids," Tech. rep., Los Alamos Scientific Lab., N. Mex. (1954).
2. E. E. Meshkov, "Instability of the interface of two gases accelerated by a shock wave," Fluid Dyn. **4**, 101–104 (1969).
3. Rayleigh, "Investigation of the character of the equilibrium of an incompressible heavy fluid of variable density," Proc. Lond. mathematical society **1**, 170–177 (1882).
4. G. I. Taylor, "The instability of liquid surfaces when accelerated in a direction perpendicular to their planes. I," Proc. Royal Soc. London. Ser. A. Math. Phys. Sci. **201**, 192–196 (1950).
5. D. H. Sharp, "An overview of Rayleigh-Taylor instability," Phys. D: Nonlinear Phenom. **12**, 3–18 (1984).
6. P. Drazin, "Kelvin–Helmholtz instability of finite amplitude," J. Fluid Mech. **42**, 321–335 (1970).
7. J. Kane, R. Drake, and B. Remington, "An evaluation of the Richtmyer-Meshkov instability in supernova remnant formation," The Astrophys. J. **511**, 335 (1999).
8. J. Holzfuss, "Surface-wave instabilities, period doubling, and an approximate universal boundary of bubble stability at the upper threshold of sonoluminescence," Phys. Rev. E **77**, 066309 (2008).
9. G. B. Goodwin and E. S. Oran, "Premixed flame stability and transition to detonation in a supersonic combustor," Combust. Flame **197**, 145–160 (2018).
10. V. Rupert, "Shock-interface interaction: current research on the Richtmyer-Meshkov problem," in *Shock Waves: Proceedings of the 18th International Symposium on Shock Waves, Held at Sendai, Japan 21–26 July 1991,* (Springer, 1992), pp. 83–94.
11. M. Brouillette, "The Richtmyer-Meshkov instability," Annu. Rev. Fluid Mech. **34**, 445–468 (2002).
12. Y. Zhou, R. J. Williams, P. Ramaprabhu, *et al.*, "Rayleigh–Taylor and Richtmyer–Meshkov instabilities: A journey through scales," Phys. D: Nonlinear Phenom. **423**, 132838 (2021).
13. E. Leinov, G. Malamud, Y. Elbaz, *et al.*, "Experimental and numerical investigation of the Richtmyer–Meshkov instability under re-shock conditions," J. Fluid Mech. **626**, 449–475 (2009).
14. R. L. Holmes, G. Dimonte, B. Fryxell, *et al.*, "Richtmyer–Meshkov instability growth: experiment, simulation and theory," J. Fluid Mech. **389**, 55–79 (1999).
15. Y. Zhou, "Rayleigh–Taylor and Richtmyer–Meshkov instability induced flow, turbulence, and mixing. II," Phys. Reports **723**, 1–160 (2017).

profile	F_1	F_2	F_3	F_4	F_6	F_8
1	0	0	0	0	0	0.08
2	0	0	0	0.08	0	0
3	0	0.08	0	0	0	0
4	0	0	0	0	0	0.075
5	0	0	0	0.075	0	0
6	0	0.075	0	0	0	0
7	0	0.0075	0	0	0.0025	0.065
8	0.0075	0	0.0025	0.065	0	0
9	0.005	0.0657	0	0	0	0
10	0	0	0	0	0	0.06
11	0	0	0	0.06	0	0
12	0	0.06	0	0	0	0
13	0	0	0	0	0	0.055
14	0	0	0	0.055	0	0
15	0	0.055	0	0	0	0
16	0	0.0075	0	0	0.0025	0.045
17	0.0075	0	0.0025	0.045	0	0
18	0.0051	0.0457	0	0	0	0
19	0	0	0	0.04	0	0
20	0	0.04	0	0	0	0

Table 2. Scaled cosine coefficients for the initial shell profile used for each profile.

16. Q. Zhang and M. J. Graham, "A numerical study of Richtmyer–Meshkov instability driven by cylindrical shocks," Phys. Fluids **10**, 974–992 (1998).
17. M. B. Prime, W. T. Buttler, S. J. Fensin, *et al.*, "Tantalum strength at extreme strain rates from impact-driven Richtmyer-Meshkov instabilities," Phys. Rev. E **100**, 053002 (2019).
18. M. B. Prime, W. T. Buttler, M. A. Buechler, *et al.*, "Estimation of metal strength at very high rates using free-surface Richtmyer–Meshkov instabilities," J. Dyn. Behav. Mater. **3**, 189–202 (2017).
19. E. C. Merritt, J. P. Sauppe, E. N. Loomis, *et al.*, "Experimental study of energy transfer in double shell implosions," Phys. Plasmas **26**, 052702 (2019).
20. K. Prestridge, P. Vorobieff, P. Rightley, and R. Benjamin, "Validation of an instability growth model using particle image velocimetry measurements," Phys. review letters **84**, 4353 (2000).
21. M. Emery, J. Gardner, R. Lehmberg, and S. Obenschain, "Hydrodynamic target response to an induced spatial incoherence-smoothed laser beam," Phys. Fluids B: Plasma Phys. **3**, 2640–2651 (1991).
22. R. Ishizaki and K. Nishihara, "Propagation of a rippled shock wave driven by nonuniform laser ablation," Phys. review letters **78**, 1920 (1997).
23. J. D. Lindl, R. L. McCrory, and E. M. Campbell, "Progress toward ignition and burn propagation in inertial confinement fusion," Phys. Today **45**, 32–40 (1992).
24. R. Taylor, A. Velikovich, J. Dahlburg, and J. Gardner, "Saturation of laser imprint on ablatively driven plastic targets," Phys. review letters **79**, 1861 (1997).

25. E. Lifshin, *X-ray Characterization of Materials* (John Wiley & Sons, 2008).

26. D. C. Swift, A. L. Kritcher, J. A. Hawreliak, *et al.*, "Absolute Hugoniot measurements from a spherically convergent shock using X-ray radiography," Rev. Sci. Instruments **89** (2018).

27. J. Rygg, O. Jones, J. Field, *et al.*, "2D x-ray radiography of imploding capsules at the National Ignition Facility," Phys. Rev. Lett. **112**, 195001 (2014).

28. M. Hossain, B. T. Nadiga, O. Korobkin, *et al.*, "High-precision inversion of dynamic radiography using hydrodynamic features," Opt. Express **30**, 14432–14452 (2022).

29. J. Radon, "Uber die bestimmung von funktionen durch ihre integralwerte längs gewisser mannigfaltigkeiten (on the determination of function from their integral value along certain manifolds)," Berichte Sächsische Akademie der Wissenschaften, Leipzig, Math.-Phys. Kl **69**, 262–267 (1917).

30. A. M. Cormack, "Representation of a function by its line integrals, with some radiological applications," J. Appl. Phys. **34**, 2722–2727 (1963).

31. L. A. Feldkamp, L. C. Davis, and J. W. Kress, "Practical cone-beam algorithm," JOSA A **1**, 612–619 (1984).

32. R. N. Bracewell and R. N. Bracewell, *The Fourier transform and its applications*, vol. 31999 (McGraw-Hill New York, 1986).

33. I. A. Elbakri and J. A. Fessler, "Statistical image reconstruction for polyenergetic x-ray computed tomography," IEEE transactions on medical imaging **21**, 89–99 (2002).

34. S. Ravishankar, J. C. Ye, and J. A. Fessler, "Image reconstruction: From sparsity to data-adaptive methods and machine learning," Proc. IEEE **108**, 86–109 (2019).

35. M. Pasha, A. K. Saibaba, S. Gazzola, *et al.*, "A computational framework for edge-preserving regularization in dynamic inverse problems," Electron. Trans. on Numer. Anal. **58**, 486–516 (2023).

36. D. F. Yu and J. A. Fessler, "Edge-preserving tomographic reconstruction with nonlocal regularization," IEEE transactions on medical imaging **21**, 159–173 (2002).

37. A. H. Delaney and Y. Bresler, "Globally convergent edge-preserving regularized reconstruction: an application to limited-angle tomography," IEEE Trans. on Image Process. **7**, 204–221 (1998).

38. M. Unberath, J.-N. Zaech, C. Gao, *et al.*, "Enabling machine learning in x-ray-based procedures via realistic simulation of image formation," Int. J. Comput. Assist. Radiol. Ssurgery **14**, 1517–1528 (2019).

39. S. Sajed, A. Sanati, J. E. Garcia, *et al.*, "The effectiveness of deep learning vs. traditional methods for lung disease diagnosis using chest x-ray images: A systematic review," Appl. Soft Comput. p. 110817 (2023).

40. C. Sun, Y. Liu, and H. Yang, "Degradation-aware deep learning framework for sparse-view CT reconstruction," Tomography **7**, 932–949 (2021).

41. Z. Huang, M. Klasky, T. Wilcox, and S. Ravishankar, "Physics-driven learning of Wasserstein GAN for density reconstruction in dynamic tomography," Appl. Opt. **61**, 2805–2817 (2022).

42. A. Dosovitskiy, L. Beyer, A. Kolesnikov, *et al.*, "An image is worth 16x16 words: Transformers for image recognition at scale," in *International Conference on Learning Representations,* (2021).

43. A. Vaswani, N. Shazeer, N. Parmar, *et al.*, "Attention is all you need," in *Advances in Neural Information Processing Systems,* vol. 30 I. Guyon, U. V. Luxburg, S. Bengio, *et al.*, eds. (Curran Associates, Inc., 2017).

44. X. Xu, M. Klasky, J. A. Fessler, *et al.*, "An end-to-end learning approach for subpixel edge feature extraction," Radiogr. Imaging Tomogr. Summer Symp. (2023).

45. M. Berger, J. Hubbell, S. Seltzer, *et al.*, "XCOM: Photon cross sections database (version 1.5)," NIST Stand. Ref. Database **8**, 87–3597 (2010).

46. M. Sun and J. M. Star-Lack, "Improved scatter correction using adaptive scatter kernel superposition," Phys. Med. Biol. **55**, 6695–6720 (2010).

47. M. T. McCann, M. L. Klasky, J. L. Schei, and S. Ravishankar, "Local models for scatter estimation and descattering in polyenergetic X-ray tomography," Opt. Express **29**, 29423–29438 (2021).

48. I. Elbakri and J. Fessler, "Statistical image reconstruction for polyenergetic X-ray computed tomography," IEEE Trans. on Med. Imaging **21**, 89–99 (2002).

49. G. R. Myers, A. M. Kingston, T. K. Varslot, *et al.*, "Dynamic tomography with a priori information," Appl. Opt. **50**, 3685–3690 (2011).

50. S. Bonnet, A. Koenig, S. Roux, *et al.*, "Dynamic X-ray computed tomography," Proc. IEEE **91**, 1574–1587 (2003).

51. L. Desbat, S. Rit, R. Clackdoyle, *et al.*, "Algebraic and analytic reconstruction methods for dynamic tomography," in *2007 29th Annual International Conference of the IEEE Engineering in Medicine and Biology Society,* (IEEE, 2007), pp. 726–730.

52. C. Jailin and S. Roux, "Dynamic tomographic reconstruction of deforming volumes," Materials **11**, 1395 (2018).

53. E. F. Toro, *Riemann solvers and numerical methods for fluid dynamics: a practical introduction* (Springer Science & Business Media, 2013).

54. P. D. Bello-Maldonado, T. V. Kolev, R. N. Rieben, and V. Z. Tomov, "A matrix-free hyperviscosity formulation for high-order ale hydrodynamics," Comput. & Fluids **205**, 104577 (2020).

55. Hertel, E. S. Jr. and Kerley, G. I., "CTH Reference Manual: The Equation of State Package," report SAND98-0947, Sandia National Laboratories (1998).

56. W. van Aarle, W. J. Palenstijn, J. De Beenhouwer, *et al.*, "The ASTRA toolbox: A platform for advanced algorithm development in electron tomography," Ultramicroscopy **157**, 35–47 (2015).

57. D. P. Kingma and M. Welling, "Auto-encoding variational Bayes," CoRR **abs/1312.6114** (2013).

58. L. P. Cinelli, M. A. Marins, E. A. B. Da Silva, and S. L. Netto, *Variational methods for machine learning with applications to deep networks* (Springer, 2021).
59. D. P. Kingma, S. Mohamed, D. Jimenez Rezende, and M. Welling, "Semi-supervised learning with deep generative models," Adv. Neural Inf. Process. Syst. **27** (2014).

Reconstructions and Testing Set Structural Similarity for each Profile
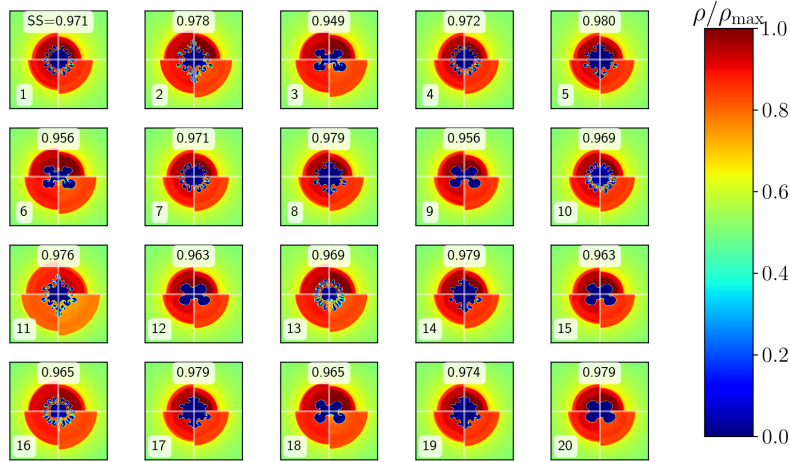
(a) Mass-Conserving Transformer: Examples of density reconstructions for each inner surface perturbation profile sorted by the profile ensemble average Structural Similarity in the testing set. The plots are labeled by their profile number and the corresponding profile ensemble average Structural Similarity.

Reconstruction Error and Testing Set RSME for each Profile
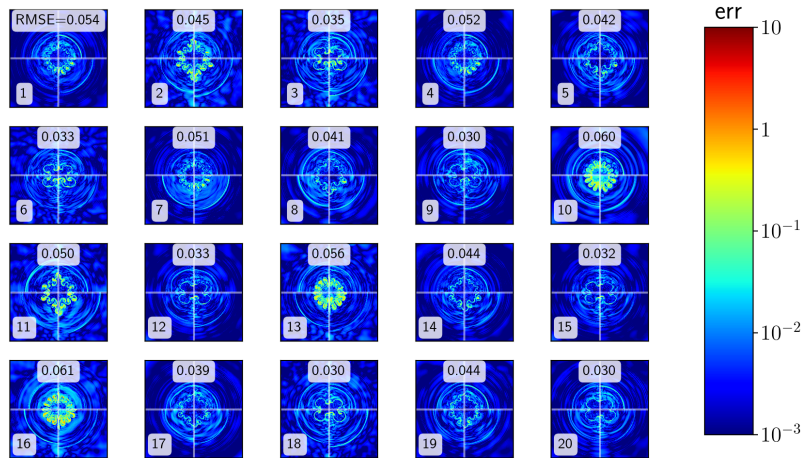
(b) Mass-Conserving Transformer: Corresponding errors between the model and the ground truth on a log scale for the above reconstructions, labeled by their profile number and the corresponding profile ensemble average RSME in g/cc.

Fig. 10. Mass-Conserving Transformer: (a) Density reconstructions and (b) their errors for a random choice of simulation parameters corresponding to each inner surface perturbation profile. Each plot shows quarter planes corresponding data at each of the four times in the sequence counter-clockwise from the first quadrant.
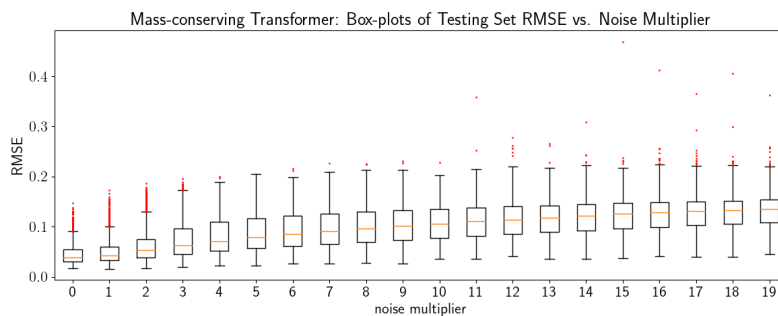
Fig. 11. Box-plots of RSME (g/cc) evaluated on the testing set corresponding to noise multipliers $0, 1, \ldots, 19$. Each box extends from the first quartile to the third quartile of the data with an orange line representing the median. The whiskers extend from the box to the farthest data point lying within 1.5x the inter-quartile range from the box. The red dots represent points outside of the whiskers.
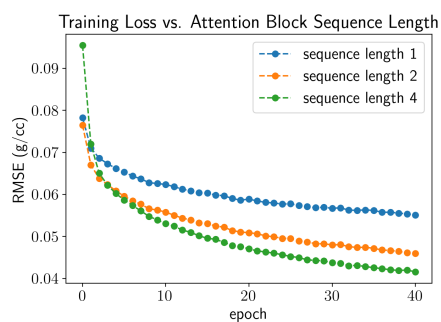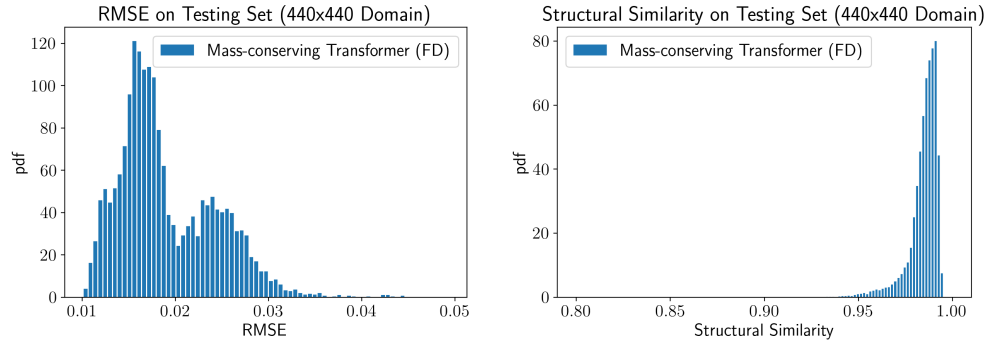

Fig. 12. Comparison of training loss when the attention blocks of the mass-conserving transformer are fully connected (sequence length 4), connected only between the first two and latter two times (sequence length 2), and fully disconnected (sequence length 1). For consistency between methods, RMSE is evaluated on the entire sequence of 4 density reconstructions.

Architecture	RMSE (g/cc)			Structural Similarity		
	min	average	max	min	average	max
Mass Conserving Transformer	0.010	0.019	0.049	0.92	0.98	0.99

Fig. 13. Histogram of root-mean-squared errors (RMSE) (top left) and structural similarity (top right) between the density reconstruction and ground truth for the testing set for the Mass-conserving transformer trained on the entire domain. Bottom: table of summary statistics for the above histograms.
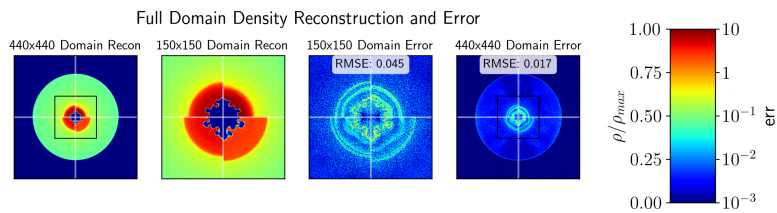
Fig. 14. Example of full density reconstructions and their corresponding errors produced by the Mass-Conserving Transformer. The input shock features are polluted with simulated noise from the radiograph-to-feature network.
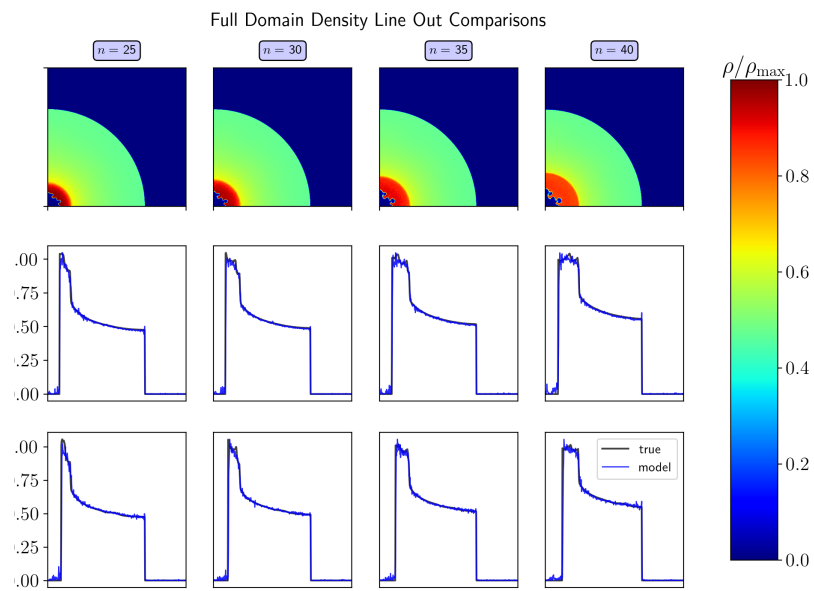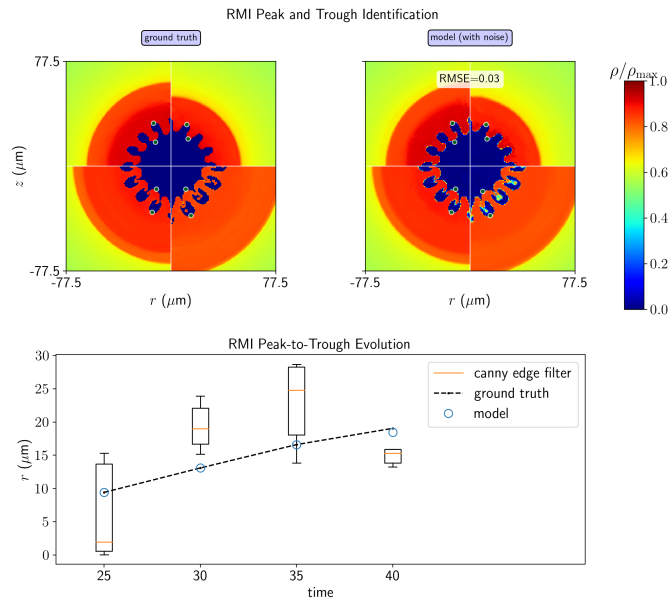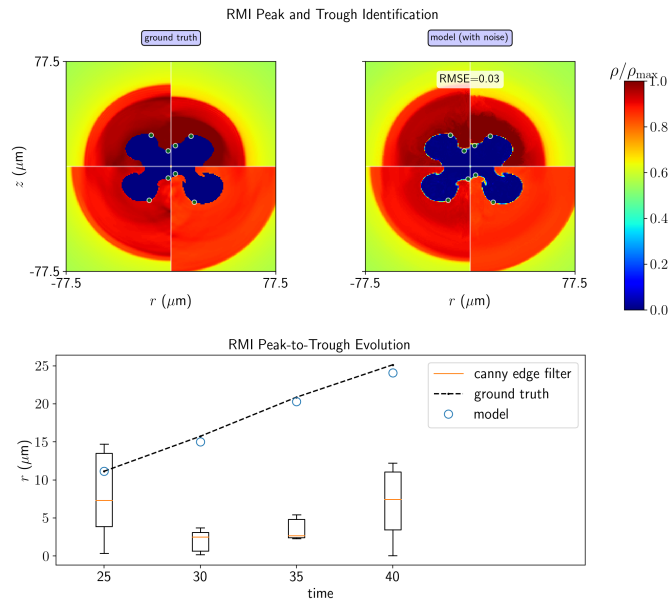
Fig. 15. Plot of reconstruction and horizontal and vertical density line plots produced by the Mass-Conserving Transformer trained on the entire domain. The input shock features are polluted with simulated noise from the radiograph-to-feature network.

(a) High frequency RMI mode example (profile 1).

(b) Low frequency RMI mode example (profile 9).

Fig. 16. Top plots: density fields and identified peak and trough points of the RMI (green markers) for the ground truth and reconstructions using inputs polluted with simulated noise from the radiograph-to-feature network. Bottom plots: evolution of the maximum RMI peak-to-trough radial distance for the ground truth and reconstructions corresponding to the above plots.